High Power Laser Science and Engineering, (2024), Vol. 12, e6, 8 pages.
doi:10.1017/hpl.2023.90

HIGH POWER LASER SCIENCE AND ENGINEERING

RESEARCH ARTICLE

Design, performance and application of a line-imaging velocity interferometer system for any reflector coupled with a streaked optical pyrometer system at the Shenguang-II upgrade laser facility

Dawei Yuan[1,2], Shaojun Wang[3,7], Huigang Wei[1], Haochen Gu[3,7], Yu Dai[3,7], Jiayong Zhong[2,5], Yutong Li[3,6,7,8], Gang Zhao[1], and Jie Zhang[3,4,6]

[1] *Key Laboratory of Optical Astronomy, National Astronomical Observatories, Chinese Academy of Sciences, Beijing, China*

[2] *Institute of Frontiers in Astronomy and Astrophysics of Beijing Normal University, Beijing, China*

[3] *Beijing National Laboratory for Condensed Matter Physics, Institute of Physics, Chinese Academy of Sciences, Beijing, China*

[4] *Key Laboratory for Laser Plasmas (MOE) and School of Physics and Astronomy, Shanghai Jiao Tong University, Shanghai, China*

[5] *Department of Astronomy, Beijing Normal University, Beijing, China*

[6] *Collaborative Innovation Center of IFSA, Shanghai Jiao Tong University, Shanghai, China*

[7] *School of Physical Sciences, University of Chinese Academy of Sciences, Beijing, China*

[8] *Songshan Lake Materials Laboratory, Dongguan, China*

(Received 30 August 2023; revised 4 November 2023; accepted 10 November 2023)

Abstract

The velocity interferometer system for any reflector (VISAR) coupled with a streaked optical pyrometer (SOP) system is used as a diagnostic tool in inertial confinement fusion (ICF) experiments involving equations of state and shock timing. To validate the process of adiabatically compressing the fuel shell through precise tuning of shocks in experimental campaigns for the double-cone ignition (DCI) scheme of ICF, a compact line-imaging VISAR with an SOP system is designed and implemented at the Shenguang-II upgrade laser facility. The temporal and spatial resolutions of the system are better than 30 ps and 7 μm, respectively. An illumination lens is used to adjust the lighting spot size matching with the target size. A polarization beam splitter and λ/4 waveplate are used to increase the transmission efficiency of our system. The VISAR and SOP work at 660 and 450 nm, respectively, to differentiate the signals from the scattered lights of the drive lasers. The VISAR can measure the shock velocity. At the same time, the SOP system can give the shock timing and relative strength. This system has been used in different DCI campaigns, where the generation and propagation processes of multi-shock are carefully diagnosed.

Keywords: double-cone ignition; streaked optical pyrometer; velocity interferometer system for any reflector

1. Introduction

The velocity interferometer system for any reflector (VISAR)[1–4] coupled with a streaked optical pyrometer (SOP)[5–7] has been used as a diagnostic tool in inertial confinement fusion (ICF)[8–12], such as in shock-timing and equation of state (EOS) experiments. The VISAR diagnoses the evolution of moving surface velocity by measuring the shifted interference fringes, while the SOP analyzes the radiance temperature of a shocked thin layer by comparing the measured self-emission intensity with the brightness temperature from a standard Plankian blackbody radiator. In shock-timing experiments, a multi-shock compression scheme is proposed to achieve a high areal density under the low entropy conditions[13,14]. The study of the precise shock timing and strength is primarily important. The VISAR and SOP have shown the capability

Correspondence to: Dawei Yuan, Key Laboratory of Optical Astronomy, National Astronomical Observatories, Chinese Academy of Sciences, Beijing 100101, China. Email: dwyuan@bao.ac.cn; Yutong Li, Beijing National Laboratory for Condensed Matter Physics, Institute of Physics, Chinese Academy of Sciences, Beijing 100190, China. Email: ytli@iphy.ac.cn; Gang Zhao, Key Laboratory of Optical Astronomy, National Astronomical Observatories, Chinese Academy of Sciences, Beijing 100101, China. Email: gzhao@bao.ac.cn; Jie Zhang, Key Laboratory for Laser Plasmas (MOE) and School of Physics and Astronomy, Shanghai Jiao Tong University, Shanghai 200240, China. Email: jzhang1@sjtu.edu.cn

of measuring the shock velocity evolution and relative strength, successfully observing the multi-shock overtaking and merging process[8,15]. In EOS experiments, the material response at extreme pressure is important for hydrodynamic simulation for target design and ignition physics. Shock or ramp compression experiments are performed to examine and calibrate the EOS database derived from theoretical models[16,17]. The use of the VISAR and SOP simultaneously measuring the shock/particle velocity and temperature can well define the materials' EOS.

Here we report on a newly built line-imaging VISAR and SOP system. In order to verify the feasibility of our designed optical system, a prototype of the VISAR with two channels with different sensitivities was set up at the Shenguang-II laser facility, where the interaction of multiple shocks in a planar target with a ramp-pulse was successfully observed[18]. In an upgrade version performed at the Shenguang-II upgrade (SG-II UP) laser facility[19], we modified the optical design by coupling the SOP optical path to the VISAR. The temporal and spatial resolutions of the system are better than 30 ps and 7 μm, respectively. To maximize the use of the available VISAR laser energy to observe the signal from the weakly reflecting shock, we performed two modifications to the optical design. The first is the change of an illumination lens to adjust the lighting spot size (from 200 to 1000 μm) to match with the target size. It ensures that more VISAR laser energy is used to illuminate the target. The second is the employment of the combination of a polarization beam splitter (PBS) and λ/4 waveplate replacing the beam splitter (BS) used at the SG-III prototype[4], OMEGA[2] and NIF[3]. It improves the transmission efficiency of our system. In addition, a standard timing reference containing 10 pulses is transmitted by an optical fiber to the streak camera (SC). This system has been commissioned in different runs of the experimental campaign of the double-cone ignition (DCI) scheme[20,21]. Multi-shock compression in the planar target and quasi-isentropic compression inside a shell-in-cone target are successfully observed by the VISAR and SOP.

This paper mainly presents the details of the system. Section 2 describes the system layout, including design and implementation at the SG-II UP laser facility. Section 3 shows the applications in the recent runs of the DCI campaign. Finally, concluding remarks are given in Section 4.

2. System layout

Figure 1 shows the location of the line-imaging VISAR and SOP system installed on a 2.4-m-diameter vacuum chamber at the SG-II UP laser facility. Four drive laser beams from the upper hemisphere are focused onto the target (here only one drive laser beam is shown in Figure 1(a)). The collected signals from the shocked target are transported onto the diagnostic table. The overall appearance of the VISAR and SOP system, which has two floors (upper and lower), is shown in Figure 1(b). All optical elements are compacted at the table with dimensions of 1.8 m (length) × 1.2 m (width) × 0.4 m (height). The entire optical path is about 9 m.

Figure 2 displays the optical design of the VISAR and SOP system. The VISAR probe laser beam goes through the illumination lens, PBS, special beam splitter (SBS), L1 and λ/4 before reaching the rear side of the target. The combined signal consisting of the reflected probe laser and

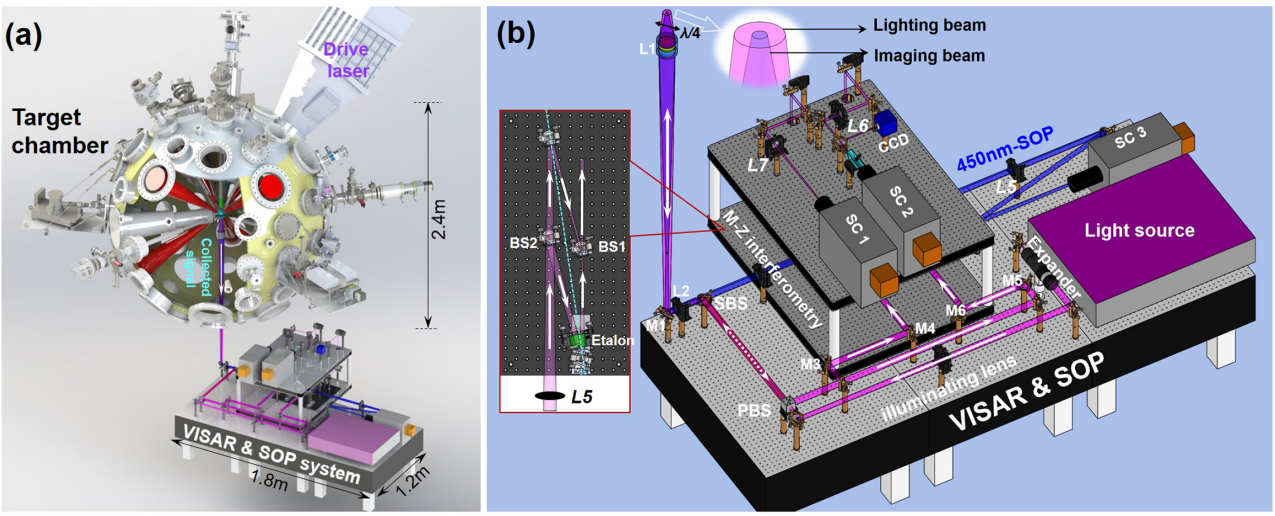

Figure 1. (a) Location and implementation of the VISAR and SOP system. (b) Schematic layout of the system including two channels for the VISAR with two sensitivities (red in the upper table) and one channel for the SOP (blue in the lower table). The inset shows one of the Mach–Zehnder interferometer assemblies.

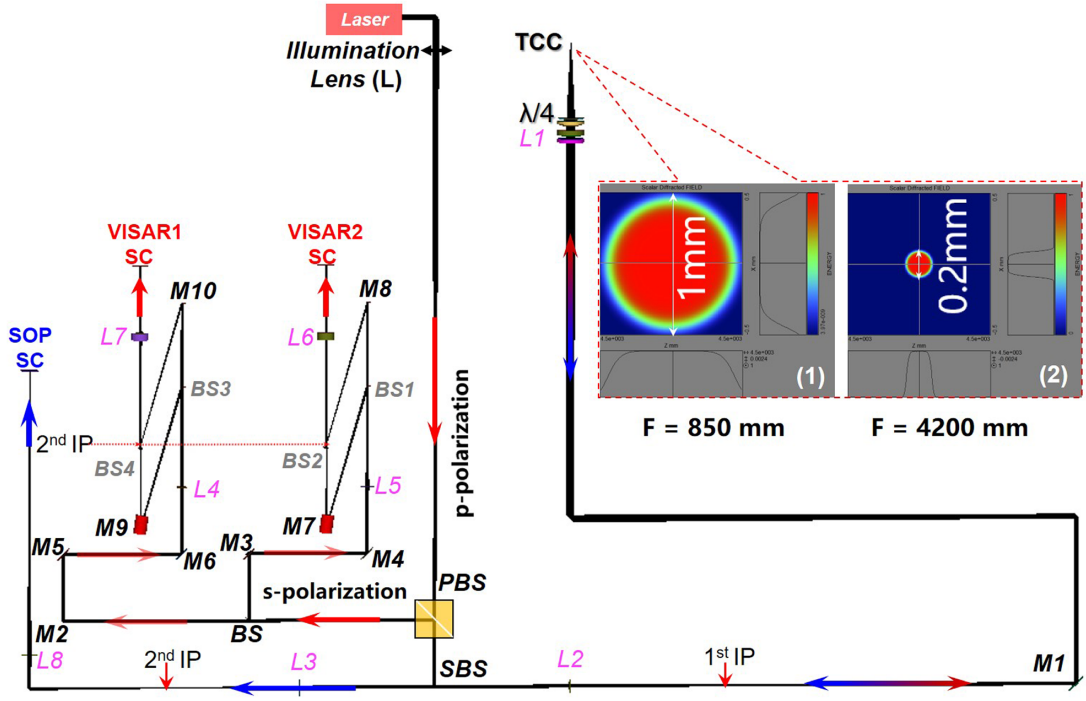

Figure 2. The optical ray tracing of the system. The collected signal lights including the reflected VISAR probe laser beam and the self-emission are transported onto the optical table. When it arrives at the SBS, the signal is split into two recording paths, the interferometer section (red arrow) and the SOP section (blue arrow). The insets show the designed spot sizes with different illumination lenses at the same position. L, lens; M, mirror; IP, imaging position; BS, beam splitter; PBS, polarization beam splitter; SBS, special beam splitter (dichroic mirror); TCC, target chamber center; SC, streak camera.

the self-emission lights is collected by a specially designed imaging lens, L1. When these signals arrive at the SBS, the reflected probe carrying velocity information is reflected into the VISAR line, while the self-emission is transmitted into the SOP line. Finally, these signals are imaged at the slit of the SCs. In order to spatially resolve along any orientation on the target, the Dove prisms are placed at the front of the SCs to correctly rotate the image. In general, this system integrates the following components: the VISAR probe laser, illumination sub-system, imaging sub-system, Mach–Zehnder (M-Z) interferometers with different sensitivities, SOP sub-system, timing reference and optical SCs. Here we introduce them in detail.

2.1. VISAR probe laser

A compact neodymium-doped yttrium aluminum garnet (Nd:YAG) laser system with high stability, high beam quality and tunable pulse width is built as the VISAR illuminating light source[22]. This laser can deliver a maximum energy of 4.5 mJ with a square waveform of approximately 50 ns (full width at half maximum, FWHM), achieved by an arbitrary waveform generator. Here we use the probe laser working at 660 nm (2ω) to differentiate the signals of the VISAR from the drive laser (3ω) and unconverted 1ω and 2ω light. A narrow line width of less than 5.8×10^{-8} nm ensures the visibility of the interference fringes with a high contrast. The probe laser can run either with a single shot for operation in the experiment or at a repetition rate (1–5 Hz) for alignment.

2.2. Illumination sub-system

The traditional illumination system used in the VISAR is a probe laser beam coupled with a BS[2–4]. The probe laser goes through the BS to arrive at the target chamber center (TCC), where only half of the laser energy is delivered to the target. When the back-reflected light goes through the BS again, only half of the signal energy is delivered into the VISAR recording passage. This means that only 25% of the probe laser energy is used. As shown in Figure 2, we improve the illumination scheme with a PBS and a 1/4 waveplate (λ/4). A p-polarized probe laser beam has an overall near-100% transmission before arriving at the rear side of the target. The retro-reflected beam through the λ/4 waveplate undergoes a polarization rotation and becomes an s-polarized beam. This s-polarized beam can be totally reflected into the M-Z interferometer and recorded by the SCs. This improvement has two advantages: one is to increase the transmission efficiency by threefold, helping us to measure the weaker shock signal (see below), and the other is to enhance the signal-to-noise ratio since only the s-polarized signal can pass through the PBS and be injected into the VISAR line.

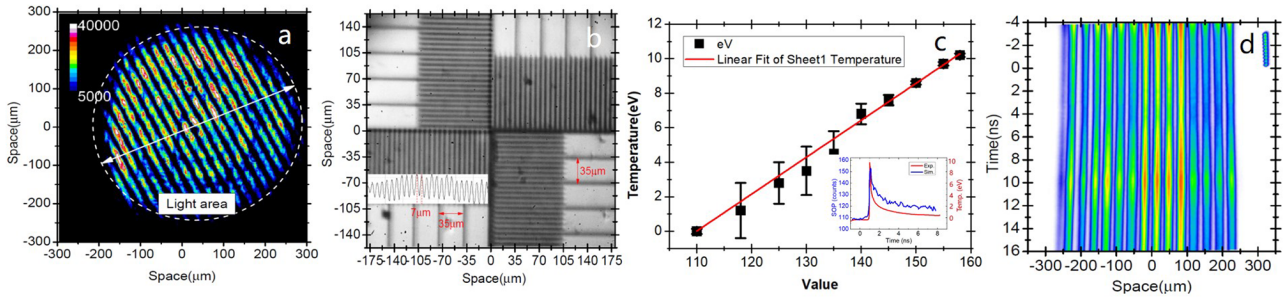

Figure 3. Typical parameters of the VISAR in the DCI campaign. (a) A 500-μm-diameter light-spot with imposed interferometer fringes is obtained by using an illumination lens with $F = 2200$ mm. (b) The spatial resolution of the whole system is better than 7 μm using the tested reticle placing at the TCC. (c) The obtained relationship between the emission temperature and the measured count value. (d) The static fringes in the field of view are swept by the SC.

In order to study the compression process in different targets, a variable lighting spot size of 200–1000 μm is designed to match with the target size by using an illumination lens (L). This optical design ensures that more VISAR laser energy can be used to illuminate the target. The lighting spot size can be easily changed by choosing a proper focusing length of the illumination lenses. The optical design is shown in the insets of Figure 2. A 200-μm-diameter light-spot is obtained when we use an illumination lens with $F = 4200$ mm, while a 1000-μm-diameter light-spot is obtained for $F = 850$ mm. Figure 3(a) shows a typical illumination spot size used in the DCI campaigns (DCI-R6). A 500-μm-diameter spot with imposed interferometry fringes is obtained with an illumination lens with $F = 2200$ mm placed at a distance of 900 mm from the VISAR illuminating light source.

2.3. *Imaging sub-system*

As shown in Figure 2, the whole imaging system consists of three stages. The first imaging lens L1 is the core of the whole imaging system, determining the spatial resolution. L1 is an achromatic lens combination consisting of three parts: the first one is a double convex lens, while the other two are concave–convex lenses with different curvatures. The equivalent focal length of L1 is 258 mm with the effective diameter of 78 mm (corresponding to F number of 3.3). It is placed at 275 mm away from the TCC to collect the reflected light and self-emission. The image is then transferred to the fixed position with a magnification of 15×, which is 4400 mm away from the TCC. The second is an image transfer system with a magnification of 1×, delivering the intermediate image to the optical table. One is transferred to the M-Z interferometer table imaging at BS2 and BS4 (second imaging position (IP)), while the other is transferred to the SOP table (second IP). The third-stage image is placed in front of the slit of the SC with a magnification of 3×. The imaging system yields an overall magnification of 45× with a spatial resolution better than 7 μm (see Figure 3(b)). This design of the three-stage imaging system allows us to diagnose targets with different sizes by simply changing the magnification of the third-stage image.

2.4. *Mach–Zehnder interferometers*

The inset of Figure 1(b) shows the M-Z interferometer assembly, which is built on an optical breadboard. The mirrors and splitters are set at designed angles with the optical axis on their centers. The arrangement is symmetric to eliminate delays induced by the optical elements. The observation of white light interferometer fringes that appear at the center of the view can retain the optical path difference between two arms within 1.5 μm. A standard etalon is placed in one arm, providing a known phase. The etalon and mirror M7/M9 are placed on a motorized high-resolution translation stage. A small angle of approximately 5° between the interferometer arms matches the etalon diameter of 25.4 mm to ensure the collected light freely passes through the etalon. The phase change from Doppler shifts is accumulated at this preset phase and leads to fringe shift, which can be detected by the SCs.

A servo-controlled mirror assembly (M3 & M4, M5 & M6) is used to align the collected light direction. These collected lights are split at BS1/BS3 and then recombined at BS2/BS4. The formed fringe pattern from the interferometer is imposed on the target image. By adjusting BS2/BS4, we can precisely control the fringe spacing and angle with respect to the target orientation. To achieve a high signal-to-noise ratio, all optical mirrors in the VISAR passage are high-reflection coated for 660 ± 5 nm.

In order to measure the velocities of the compressed shocks in the experiments, we design two M-Z interferometers with different sensitivities (also called VPF, velocity per fringe), which are determined by the etalon thickness. The VPF can be expressed as $\mathrm{VPF} = \frac{\lambda c}{4h(n-1/n)(1+\delta_0)}$, where λ is the wavelength of the VISAR laser, h is the etalon thickness, c is the velocity of light and n and σ_0 are determined by the dispersion of the etalon glass. Here we choose vacuum VPFs

of 4.071 and 11.093 km/s to measure the designed multi-shock velocity.

2.5. SOP sub-system

The SOP system shares the first imaging system and the second imaging system. Due to the measured wavelength of the self-emission (450 nm) being different from the VISAR laser (660 nm), both lenses L1 and L2 are achromatic. The self-emission signal from the shocked material is collected and imaged at 4400 mm away from the TCC by lens L1. Then, it is transferred to the optical table by lens L2. After that, the self-emission signal directly passes through the SBS and is finally imaged on the slit of another SC by lens L3. All the optical mirrors in the SOP passage are high-reflection coated for 450 ± 5 nm. In addition, a narrow filter (FWHM of 2 nm) with a central wavelength of 450 nm is placed in front of the SC slit, whose width is fixed at 200 μm.

The SOP system has been widely applied in temperature measurement. Here we introduce a qualitative calibration method to help us distinguish the shock timing and relative strength. The basic idea is to compare the measured self-emission signal intensity (I) with the simulated temperature (T). Firstly, we choose aluminum (Al) as the target material because of its well-known EOS. Secondly, a standard nanosecond square pulse is used as the drive laser profile. A typical comparison result is shown in the inset of Figure 3(c), where a shock is quickly generated when the laser is ablating the Al target and then decays with time. By comparing the evolution of the detected signal intensity with the simulated temperature, we get a rough relationship of T[eV] = 0.225I[counts] – 24.75, as shown in Figure 3(c). This calibrated temperature represents the relative strength of compression shock. Although the current SOP system cannot give an accurate temperature, it is useful to measure the shock timing and shock strength in our DCI campaigns. In the future, we will calibrate and verify this system using two standard Plankian blackbody radiators, as proposed in Ref. [7].

2.6. Streak cameras and timing reference

The VISAR and SOP are equipped with three high-dynamic-range SCs[23], which are manufactured by the Xi'an Institute of Optics and Precision Mechanics (XIOPM), Chinese Academy of Sciences (CAS). Each SC incorporates a streak tube with S20 photocathodes. The dynamic range is up to 9000. The SCs have five temporal sweeping windows of 5, 10, 20, 50 and 100 ns. The range of the temporal resolution is from 30 to100 ps, depending on the sweep rate of the SC. The charge-coupled device of the SCs is 16 bit with an unbinned 2048 × 2048 pixel array. The horizontal dimension of the array corresponds to the slit length of 13.3 mm, and the vertical dimension of the slit width of 4 mm. The detected signal intensity by the SCs can be simply expressed as $I = I_0\beta\eta$, where I_0 is the reflected VISAR laser intensity or the self-emission intensity, depending on the shock strength, β is the collection efficiency determined by the imaging system (~10^{-2}) and η is the transmission efficiency (90%–100% using a polarizer and λ/4 in our system). Here the VISAR laser energy is of the order of approximately mJ and the reflection efficiency by shock is typically about 10^{-3}–10^{-1}; therefore, the detected signal energy by the SCs is in the range of nJ–μJ.

As shown in Figures 4 and 5, a standard timing reference containing 10 pulses with 560 ps spacing is transmitted by optical fiber to the slit of the SCs. The fiber length is properly chosen to ensure the precise synchronization with the rising edge of the drive laser pulse.

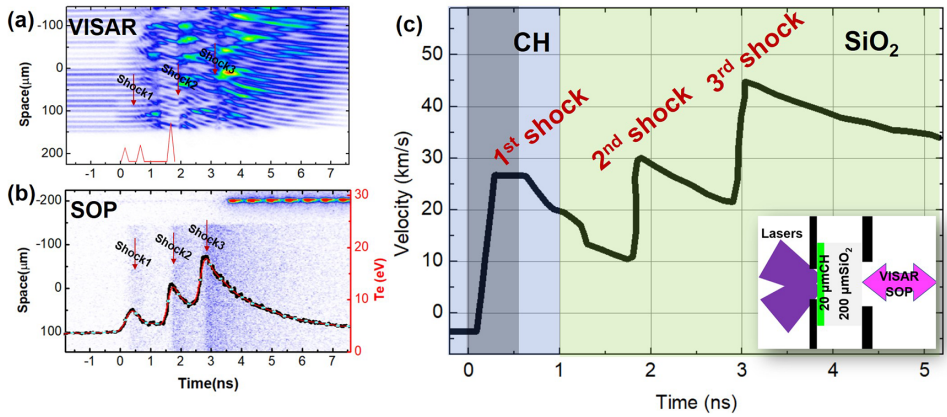

Figure 4. Multiple shocks are launched by a designed three-picket laser pulse interacting with a planar CH target. These shock timing behaviors can be clearly observed by the VISAR (a) and SOP (b). The discontinued fringes in the VISAR image and the corresponding peak intensity in the SOP image represent the generated shocks. The velocity of these shocks is obtained by extracting the shifted fringes (c). The dark region is the blinking time. The inset shows the target structure, where baffle plates are placed in the front and the rear side of the target to block the drive laser and scattered light.

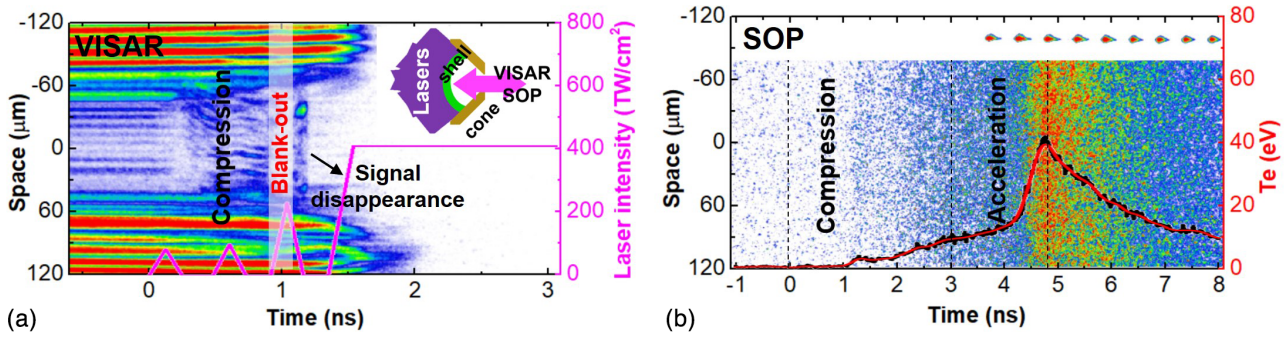

Figure 5. The compression and acceleration of the CH spherical shell inside a cone target is observed by the VISAR (a) and SOP (b). The compression is driven by a three-picket laser pulse (0–1.3 ns) and the acceleration is driven by a square main pulse (1.3–4.2 ns). The VISAR image shows that there is a blinding time roughly at approximately 1 ns during compression process. It is caused by the photoionization from the third picket interaction with the CH shell. The contrast of the region (~70–120 μm) in the upper SOP image is changed to make the timing reference clearer.

3. Applications

As an alternative method for ICF, a DCI scheme has been proposed[20]. It is composed of four controllable processes: quasi-isentropic compression, acceleration, head-on collision and fast heating. In order to obtain a low-entropy and high-areal-density compression in the DCI campaigns, a multiple shock compression scheme is proposed and conducted at the SG-II UP laser facility. In principle, this requires a sequence of shocks to coalesce simultaneously at the rear side of the target by controlling the launching time and its strength.

3.1. Multi-shock compression in a planar target

Figure 4 shows a typical result of multi-shock compression in a planar target comprising a 20 μm polystyrene ablator (CH) and a 200 μm α-quartz window (SiO_2). Four symmetrical laser beams working at 351 nm irradiate the target at a highly oblique angle of incidence of approximately 60°. Three shocks are launched by a designed laser profile consisting of three pickets with increasing energy of 58, 75 and 170 J, respectively. Each picket duration is 0.26 ns and the peak intervals are 0.46 ns and 1.0 ns.

This multi-shock evolution is successfully observed by the VISAR and SOP system. At 0.5 ns, the first shock is generated by the first picket (58 J) in the CH target with an initial velocity of 25 km/s. Between 0.5 and 1.5 ns, the fringe pattern showing a continuous decay trend represents the deceleration of the first shock (from 25 to 17 km/s). Specifically, this shock breaks through the interface into SiO_2 at 1.2 ns. The second, stronger, shock generated by the second picket (75 J) overtakes the first one with a velocity of 30 km/s at 1.7 ns. At 3 ns, the third shock generated by the third picket (170 J) with a velocity of 40 km/s is observed after overtaking the second one. The third shock continuously decelerates until it breaks through the rear side of the targe. The SOP signal also shows the same evolution of the multi-shock, where the first shock is the weakest (temperature ~8 eV) and the third shock is the strongest (temperature ~20 eV).

3.2. Quasi-isentropic compression in a shell-in-cone target

Figure 5 shows the result of a spherical compression and acceleration of the 50 μm CH spherical shell coinciding with the Au cone target. The open angle of the cone is 120°, matching with the incident angle of the drive lasers. The designed drive laser profile, shown in pink in Figure 5(a), is composed of the three pickets and a main square pulse. The three pickets have increasing energy of 58, 75 and 170 J. Each picket duration is 0.26 ns and the peak intervals are the same at 0.46 ns. The main square pulse is delivered with energy of 6.2 kJ with a duration of 2.26 ns. Four drive laser beams with designed continuous phase plates generate a spatial uniform intensity distribution to produce spherical shock compression and acceleration within the Au cone target. Here the three pickets are designed to launch multiple shocks to obtain higher areal density at low entropy. The following main square pulse accelerates the shocked spherical shell inside the cone to reach a high velocity.

It is expected that multi-shock compression within the shell-in-cone target can approach quasi-isentropic compression. This means that the fringes in the VISAR image should be continuous. However, as shown in Figure 5(a), the VISAR fringes disappear after 1.2 ns. One possible reason for this is the change in the shape of the shock during compression. A deformed shock will reflect the probe on the cone wall. Consequently, the signal cannot pass through the cone tip, causing the fringes to disappear. Therefore, the VISAR signal is sensitive to the shape of the shock. Only the perfectly spherical compression allows the reflected light to pass through the cone tip and arrive at the collection system. Although the VISAR cannot observe the whole evolution within the cone, the SOP result verifies that it is a smooth compression process with no distinct shock characteristics,

as shown in Figure 4(b). One can see that the temperature of CH in the compression process almost remains constant below 20 eV. When the acceleration process is triggered by the square main pulse, the SOP signal gets progressively stronger. At 4.6 ns, the accelerated CH shell arrives at the cone tip and the signal intensity rapidly increases from 20 to 42 eV.

4. Conclusion

A line-imaging VISAR coupled with an SOP system has been designed and installed at the SG-II UP laser facility. This system has four typical features: (1) simultaneously providing the velocity and temperature information; (2) differentiating the signal wavelengths of the system (660 nm for the VISAR and 450 nm for the SOP) from the scattered lights of the drive laser beams; (3) spatiotemporal resolution better than 7 μm and 100 ps; (4) a variable lighting spot size and a PBS coupled with a λ/4 increasing utilization efficiency of VISAR laser energy. Such improvements of the system ensure that we can obtain clear and high-contrast measurement.

In the recent runs of the DCI campaign, the generation and propagation processes of multiple-shock were carefully diagnosed. For instance, three shocks driven by three pickets in a planar target are clearly observed and the velocities were precisely measured. By comparison, a spherical compression by the same three pickets inside the cone target turns to a quasi-isentropic compression. The detailed comparison of these experimental data in different conditions will greatly deepen our understanding of the fuel compression process in ICF research.

Acknowledgements

The authors would like to thank the DCI joint team for their support of the experiment and the target fabrication. This work was supported by the Strategic Priority Research Program of the Chinese Academy of Sciences (Grant Nos. XDA25030500 and XDA25010300), the CAS Youth Interdisciplinary Team (Grant No. JCTD-2022-05), the Youth Innovation Promotion Association of the Chinese Academy of Sciences, the National Natural Science Foundation of China (Grant Nos. 11873061 and 12073043) and the National Key R&D Program of China (Grant Nos. 2022YFA1603200 and 2022YFA1603204).

References

1. L. Barker and R. Hollenbach, J. Appl. Phys. **43**, 4669 (1972).
2. P. M. Celliers, D. K. Bradley, G. W. Collins, D. G. Hicks, T. R. Boehly, and W. J. Armstrong, Rev. Sci. Instrum. **75**, 4916 (2004).
3. R. M. Malone, J. R. Brower, D. K. Bradley, G. A. Capelle, J. R. Celeste, P. M. Celliers, G. W. Collins, M. J. Eckart, J. H. Eggert, B. C. Frogget, R. L. Guyton, D. G. Hicks, M. I. Kaufman, B. J. MacGowan, S. Montelongo, E. W. Ng, R. B. Robinson, T. W. Tunnell, P. W. Watts, and P. G. Zapata, Proc. SPIE **5580**, 505 (2004).
4. F. Wang, X. Peng, S. Liu, T. Xu, L. S. Mei, X. H. Jiang, and Y. K. Ding, Rev. Sci. Instrum. **82**, 103108 (2011).
5. J. E. Miller, T. R. Boehly, A. Melchior, D. D. Meyerhofer, P. M. Celliers, J. H. Eggert, D. G. Hicks, C. M. Sorce, J. A. Oertel, and P. M. Emmel, Rev. Sci. Instrum. **78**, 034903 (2007).
6. M. C. Gregor, R. Boni, A. Sorce, J. Kendrick, C. A. McCoy, D. N. Polsin, T. R. Boehly, P. M. Celliers, G. W. Collins, D. E. Fratanduono, J. H. Eggert, and M. Millot, Rev. Sci. Instrum. **87**, 114903 (2016).
7. Z. Y. He, G. Jia, F. Zhang, X. G. Huang, Z. H. Fang, J. Q. Dong, H. Shu, J. J. Ye, Z. Y. Xie, Y. C. Tu, Q. L. Zhang, E. F. Guo, and S. Z. Fu, High Power Laser Sci. Eng. **7**, e49 (2019).
8. T. R. Boehly, V. N. Goncharov, W. Seka, M. A. Barrios, P. M. Celliers, D. G. Hicks, G. W. Collins, S. X. Hu, J. A. Marozas, and D. D. Meyerhofer, Phys. Rev. Lett. **106**, 195005 (2011).
9. H. F. Robey, J. D. Moody, P. M. Celliers, J. S. Ross, J. Ralph, S. Le Pape, L. Berzak Hopkins, T. Parham, J. Sater, and E. R. Mapoles, Phys. Rev. Lett. **111**, 065003 (2013).
10. N. Ozaki, T. Sano, M. Ikoma, K. Shigemori, T. Kimura, K. Miyanishi, T. Vinci, F. H. Ree, H. Azechi, T. Endo, Y. Hironaka, Y. Hori, A. Iwamoto, T. Kadono, H. Nagatomo, M. Nakai, T. Norimatsu, T. Okuchi, K. Otani, T. Sakaiya, K. Shimizu, A. Shiroshita, A. Sunahara, H. Takahashi, and R. Kodama, Phys. Plasmas **16**, 062702 (2009).
11. M. A. Barrios, D. G. Hicks, T. R. Boehly, D. E. Fratanduono, J. H. Eggert, P. M. Celliers, G. W. Collins, and D. D. Meyerhofer, Phys. Plasmas **17**, 056307 (2010).
12. M. A. Barrios, T. R. Boehly, D. G. Hicks, D. E. Fratanduono, J. H. Eggert, G. W. Collins, and D. D. Meyerhofer, J. Appl. Phys. **111**, 093515 (2012).
13. V. N. Goncharov, T. C. Sangster, T. R. Boehly, S. X. Hu, I. V. Igumenshchev, F. J. Marshall, R. L. McCrory, D. D. Meyerhofer, P. B. Radha, W. Seka, S. Skupsky, C. Stoeckl, D. T. Casey, J. A. Frenje, and R. D. Petrasso, Phys. Rev. Lett. **104**, 165001 (2010).
14. O. L. Landen, J. Edwards, S. W. Haan, H. F. Robey, J. Milovich, B. K. Spears, S. V. Weber, D. S. Clark, J. D. Lindl, B. J. MacGowan, E. I. Moses, J. Atherton, P. A. Amendt, T. R. Boehly, D. K. Bradley, D. G. Braun, D. A. Callahan, P. M. Celliers, G. W. Collins, E. L. Dewald, L. Divol, J. A. Frenje, S. H. Glenzer, A. Hamza, B. A. Hammel, D. G. Hicks, N. Hoffman, N. Izumi, O. S. Jones, J. D. Kilkenny, R. K. Kirkwood, J. L. Kline, G. A. Kyrala, M. M. Marinak, N. Meezan, D. D. Meyerhofer, P. Michel, D. H. Munro, R. E. Olson, A. Nikroo, S. P. Regan, L. J. Suter, C. A. Thomas, and D. C. Wilson, Phys. Plasmas **18**, 051002 (2011).
15. H. F. Robey, P. M. Celliers, J. L. Kline, A. J. Mackinnon, T. R. Boehly, O. L. Landen, J. H. Eggert, D. Hicks, S. Le Pape, D. R. Farley, M. W. Bowers, K. G. Krauter, D. H. Munro, O. S. Jones, J. L. Milovich, D. Clark, B. K. Spears, R. P. J. Town, S. W. Haan, S. Dixit, M. B. Schneider, E. L. Dewald, K. Widmann, J. D. Moody, T. D. Döppner, H. B. Radousky, A. Nikroo, J. J. Kroll, A. V. Hamza, J. B. Horner, S. D. Bhandarkar, E. Dzenitis, E. Alger, E. Giraldez, C. Castro, K. Moreno, C. Haynam, K. N. LaFortune, C. Widmayer, M. Shaw, K. Jancaitis, T. Parham, D. M. Holunga, C. F. Walters, B. Haid, T. Malsbury, D. Trummer, K. R. Coffee, B. Burr, L. V. Berzins, C. Choate, S. J. Brereton, S. Azevedo, H. Chandrasekaran, S. Glenzer, J. A. Caggiano, J. P. Knauer, J. A. Frenje, D. T. Casey, M. G. Johnson, F. H. Séguin, B. K. Young, M. J. Edwards, B. M. Van Wonterghem, J. Kilkenny, B. J. MacGowan,

J. Atherton, J. D. Lindl, D. D. Meyerhofer, and E. Moses, Phys. Rev. Lett. **108**, 215004 (2012).
16. R. F. Smith, J. H. Eggert, R. Jeanloz, T. S. Duffy, D. G. Braun, J. R. Patterson, R. E. Rudd, J. Biener, A. E. Lazicki, A. V. Hamza, J. Wang, T. Braun, L. X. Benedict, P. M. Celliers, and G. W. Collins, Nature **511**, 330 (2014).
17. J. H. Eggert, D. G. Hicks, P. M. Celliers, D. K. Bradley, R. S. McWilliams, R. Jeanloz, J. E. Miller, T. R. Boehly, and G. W. Collins, Nat. Phys. **6**, 40 (2010).
18. S. J. Wang, D. W. Yuan, H. G. Wei, F. Y. Wu, H. C. Gu, Y. Dai, Z. Zhang, X. H. Yuan, Y. T. Li, and J. Zhang, Phys. Plasmas **29**, 112701 (2022).
19. J. Q. Zhu, J. Zhu, X. C. Li, B. Q. Zhu, W. X. Ma, X. Q. Lu, W. Fan, Z. G. Liu, S. L. Zhou, G. Xu, G. W. Zhang, X. L. Xie, L. Yang, J. F. Wang, X. P. Ouyang, L. Wang, D. W. Li, P. Q. Yang, Q. T. Fan, M. Y. Sun, C. Liu, D. A. Liu, Y. L. Zhang, H. Tao, M. Z. Sun, P. Zhu, B. Y. Wang, Z. Y. Jiao, L. Ren, D. Z. Liu, X. Jiao, H. B. Huang, and Z. Q. Lin, High Power Laser Sci. Eng. **6**, e55 (2018).
20. J. Zhang, W. M. Wang, X. H. Yang, D. Wu, Y. Y. Ma, J. L. Jiao, Z. Zhang, F. Y. Wu, X. H. Yuan, Y. T. Li, and J. Q. Zhu, Philos. Trans. R. Soc. A **378**, 20200015 (2020).
21. F. Y. Wu, X. H. Yang, Y. Y. Ma, Q. Zhang, Z. Zhang, X. Y. Yuan, H. Liu, Z. D. Liu, J. Y. Zhong, J. Zheng, Y. T. Li, and J. Zhang, High Power Laser Sci. Eng. **10**, e12 (2022).
22. Q. Xiao, X. Pan, J. T. Guo, X. Q. Wang, J. F. Wang, X. Q. Jiang, G. Y. Li, X. H. Lu, X. C. Wang, S. L. Zhou, and X. C. Li, Appl. Opt. **59**, 6070 (2020).
23. J. S. Tian, High Power Laser Particle Beams **32**, 112003 (2020).